

# SEARCH FOR VERY-HIGH-ENERGY EMISSION FROM GAMMA-RAY BURSTS USING THE FIRST 18 MONTHS OF DATA FROM THE HAWC GAMMA-RAY OBSERVATORY

R. ALFARO,<sup>1</sup> C. ALVAREZ,<sup>2</sup> J.D. ÁLVAREZ,<sup>3</sup> R. ARCEO,<sup>2</sup> J.C. ARTEAGA-VELÁZQUEZ,<sup>3</sup> D. AVILA ROJAS,<sup>1</sup>  
H.A. AYALA SOLARES,<sup>4</sup> A.S. BARBER,<sup>5</sup> N. BAUTISTA-ELIVAR,<sup>6</sup> A. BECERRIL,<sup>1</sup> E. BELMONT-MORENO,<sup>1</sup> S.Y. BENZVI,<sup>7</sup>  
A. BERNAL,<sup>8</sup> J. BRAUN,<sup>9</sup> C. BRISBOIS,<sup>4</sup> K.S. CABALLERO-MORA,<sup>2</sup> T. CAPISTRÁN,<sup>10</sup> A. CARRAMINANA,<sup>10</sup> S. CASANOVA,<sup>11</sup>  
M. CASTILLO,<sup>3</sup> U. COTTI,<sup>3</sup> J. COTZOMI,<sup>12</sup> S. COUTIÑO DE LEÓN,<sup>10</sup> E. DE LA FUENTE,<sup>13</sup> C. DE LEÓN,<sup>12</sup> T. DEYOUNG,<sup>14</sup>  
R. DIAZ HERNANDEZ,<sup>10</sup> B.L. DINGUS,<sup>15</sup> M.A. DUVERNOIS,<sup>9</sup> J.C. DÍAZ-VÉLEZ,<sup>13</sup> R.W. ELLSWORTH,<sup>16</sup> K. ENGEL,<sup>17</sup>  
D.W. FIORINO,<sup>17</sup> N. FRAIJA,<sup>8</sup> J.A. GARCÍA-GONZÁLEZ,<sup>1</sup> F. GARFIAS,<sup>8</sup> M. GERHARDT,<sup>4</sup> A. GONZÁLEZ MUÑOZ,<sup>1</sup>  
M.M. GONZÁLEZ,<sup>8</sup> J.A. GOODMAN,<sup>17</sup> Z. HAMPEL-ARIAS,<sup>9</sup> J.P. HARDING,<sup>15</sup> A. HERNANDEZ-ÁLMADA,<sup>1</sup> S. HERNANDEZ,<sup>1</sup>  
B. HONA,<sup>4</sup> C.M. HUI,<sup>18</sup> P. HÜNTEMEYER,<sup>4</sup> A. IRIARTE,<sup>8</sup> A. JARDIN-BLICQ,<sup>19</sup> V. JOSHI,<sup>19</sup> S. KAUFMANN,<sup>2</sup> D. KIEDA,<sup>5</sup>  
R.J. LAUER,<sup>20</sup> W.H. LEE,<sup>8</sup> D. LENNARZ,<sup>21</sup> H. LEÓN VARGAS,<sup>1</sup> J.T. LINNEMANN,<sup>14</sup> A.L. LONGINOTTI,<sup>10</sup> G. LUIS RAYA,<sup>6</sup>  
R. LUNA-GARCÍA,<sup>22</sup> R. LÓPEZ-COTO,<sup>19</sup> K. MALONE,<sup>23</sup> S.S. MARINELLI,<sup>14</sup> O. MARTINEZ,<sup>12</sup> I. MARTINEZ-CASTELLANOS,<sup>17</sup>  
J. MARTÍNEZ-CASTRO,<sup>22</sup> H. MARTÍNEZ-HUERTA,<sup>24</sup> J.A. MATTHEWS,<sup>20</sup> P. MIRANDA-ROMAGNOLI,<sup>25</sup> E. MORENO,<sup>12</sup>  
M. MOSTAFÁ,<sup>23</sup> L. NELLEN,<sup>26</sup> M. NEWBOLD,<sup>5</sup> R. NORIEGA-PAPAQUI,<sup>25</sup> R. PELAYO,<sup>22</sup> E.G. PÉREZ-PÉREZ,<sup>6</sup> J. PRETZ,<sup>23</sup>  
Z. REN,<sup>20</sup> C.D. RHO,<sup>7</sup> C. RIVIÈRE,<sup>17</sup> D. ROSA-GONZÁLEZ,<sup>10</sup> M. ROSENBERG,<sup>23</sup> E. RUÍZ-VELASCO,<sup>1</sup> H. SALAZAR,<sup>12</sup>  
F. SALESA GREUS,<sup>11</sup> A. SANDOVAL,<sup>1</sup> M. SCHNEIDER,<sup>27</sup> H. SCHOORLEMMER,<sup>19</sup> G. SINNI,<sup>15</sup> A.J. SMITH,<sup>17</sup> R.W. SPRINGER,<sup>5</sup>  
P. SURAJBALI,<sup>19</sup> I. TABOADA,<sup>21</sup> O. TIBOLLA,<sup>2</sup> K. TOLLEFSON,<sup>14</sup> I. TORRES,<sup>10</sup> T.N. UKWATTA,<sup>15</sup> G. VIANELLO,<sup>28,\*</sup>  
T. WEISGARBER,<sup>9</sup> S. WESTERHOFF,<sup>9</sup> J. WOOD,<sup>9</sup> T. YAPICI,<sup>14</sup> P.W. YOUNK,<sup>15</sup> A. ZEPEDA,<sup>24</sup> AND H. ZHOU<sup>15</sup>  
(THE HAWC COLLABORATION)

<sup>1</sup>*Instituto de Física, Universidad Nacional Autónoma de México, Ciudad de México, Mexico*

<sup>2</sup>*Universidad Autónoma de Chiapas, Tuxtla Gutiérrez, Chiapas, Mexico*

<sup>3</sup>*Universidad Michoacana de San Nicolás de Hidalgo, Morelia, Mexico*

<sup>4</sup>*Department of Physics, Michigan Technological University, Houghton, MI, USA*

<sup>5</sup>*Department of Physics and Astronomy, University of Utah, Salt Lake City, UT, USA*

<sup>6</sup>*Universidad Politécnica de Pachuca, Pachuca, Hidalgo, Mexico*

<sup>7</sup>*Department of Physics & Astronomy, University of Rochester, Rochester, NY, USA*

<sup>8</sup>*Instituto de Astronomía, Universidad Nacional Autónoma de México, Ciudad de México, Mexico*

<sup>9</sup>*Department of Physics, University of Wisconsin-Madison, Madison, WI, USA*

<sup>10</sup>*Instituto Nacional de Astrofísica, Óptica y Electrónica, Puebla, Mexico*

<sup>11</sup>*Instytut Fizyki Jadrowej im Henryka Niewodniczańskiego Polskiej Akademii Nauk, Krakow, Poland*

<sup>12</sup>*Facultad de Ciencias Físico Matemáticas, Benemérita Universidad Autónoma de Puebla, Puebla, Mexico*

<sup>13</sup>*Departamento de Física, Centro Universitario de Ciencias Exactas e Ingenierías, Universidad de Guadalajara, Guadalajara, Mexico*

<sup>14</sup>*Department of Physics and Astronomy, Michigan State University, East Lansing, MI, USA*

<sup>15</sup>*Physics Division, Los Alamos National Laboratory, Los Alamos, NM, USA*

<sup>16</sup>*School of Physics, Astronomy, and Computational Sciences, George Mason University, Fairfax, VA, USA*

<sup>17</sup>*Department of Physics, University of Maryland, College Park, MD, USA*

<sup>18</sup>*NASA Marshall Space Flight Center, Astrophysics Office, Huntsville, AL, USA*

<sup>19</sup>*Max-Planck Institute for Nuclear Physics, 69117 Heidelberg, Germany*

<sup>20</sup>*Department of Physics and Astronomy, University of New Mexico, Albuquerque, NM, USA*

<sup>21</sup>*School of Physics and Center for Relativistic Astrophysics, Georgia Institute of Technology, Atlanta, GA, USA*

<sup>22</sup>*Centro de Investigación en Computación, Instituto Politécnico Nacional, Ciudad de México, Mexico*

<sup>23</sup>*Department of Physics, Pennsylvania State University, University Park, PA, USA*

<sup>24</sup>*Physics Department, Centro de Investigación y de Estudios Avanzados del IPN, Ciudad de México, Mexico*

<sup>25</sup>*Universidad Autónoma del Estado de Hidalgo, Pachuca, Mexico*

<sup>26</sup>*Instituto de Ciencias Nucleares, Universidad Nacional Autónoma de México, Ciudad de México, Mexico*

<sup>27</sup>*Santa Cruz Institute for Particle Physics, University of California, Santa Cruz, Santa Cruz, CA, USA*

<sup>28</sup>*Department of Physics, Stanford University, Stanford, CA, USA*

(Received 2017 April 12; Revised 2017 May 24; Accepted 2017 May 25)

Submitted to ApJ

### ABSTRACT

The High Altitude Water Cherenkov (HAWC) Gamma-ray Observatory is an extensive air shower detector operating in central Mexico, which has recently completed its first two years of full operations. If for a burst like GRB 130427A at a redshift of 0.34 and a high-energy component following a power law with index 1.66, the high-energy component is extended to higher energies with no cut-off other than from extragalactic background light attenuation, HAWC would observe gamma rays with a peak energy of  $\sim 300$  GeV. This paper reports the results of HAWC observations of 64 gamma-ray bursts (GRBs) detected by *Swift* and *Fermi*, including three GRBs that were also detected by the Large Area Telescope (*Fermi*-LAT). An ON/OFF analysis method is employed, searching on the time scale given by the observed light curve at keV–MeV energies and also on extended time scales. For all GRBs and time scales, no statistically significant excess of counts is found and upper limits on the number of gamma rays and the gamma-ray flux are calculated. GRB 170206A, the third brightest short GRB detected by the Gamma-ray Burst Monitor on board the *Fermi* satellite (*Fermi*-GBM) and also detected by the LAT, occurred very close to zenith. The LAT measurements can neither exclude the presence of a synchrotron self-Compton (SSC) component nor constrain its spectrum. Instead, the HAWC upper limits constrain the expected cut-off in an additional high-energy component to be less than 100 GeV for reasonable assumptions about the energetics and redshift of the burst.

*Keywords:* gamma-ray burst: general — gamma rays: general

\* Contact author for the LAT collaboration: Giacomo Vianello (giacomov@stanford.edu)

## 1. INTRODUCTION

After the discovery of gamma-ray bursts (GRBs; Klebesadel et al. 1973) more than a hundred models have been proposed to explain their origins (e.g. Nemiroff 1994). Despite these efforts and a lot of progress in recent years, the details of the emission mechanisms are still poorly understood. GRBs have a prompt emission phase that typically lasts from  $\sim 10^{-2}$  s to  $\sim 10^3$  s. The light curve in the keV–MeV range is irregular, diverse and complex, with no two GRBs being alike. After the prompt phase, the X-ray light curve becomes more regular and follows a “canonical” light curve that is comparable between bursts (O’Brien et al. 2006). It transitions into a long and smooth decay, which can be studied using multi-wavelength observations. The emission of GRBs can be explained by a collimated, relativistic outflow (the so-called fireball model; for a review see e.g. Piran 1999). Relativistic ejecta propagating at various velocities can collide in the outflow and create internal shocks. The interaction of outflowing material with the surrounding medium can create external shocks (forward and reverse).

GRBs are classified into two main groups according to the duration of their prompt emission, which is measured as  $T_{90}$ , the central time interval in which 90% of the total fluence is detected (Kouveliotou et al. 1993). The duration of long GRBs is greater than two seconds, while short GRBs are shorter than two seconds. Since some long GRBs are also associated with Type Ib/Ic core-collapse supernovae (Galama et al. 1998), the core collapse of a rapidly rotating star (collapsar; Woosley 1993) is a likely candidate for long GRBs. Short GRBs are generally attributed to the merger of two compact stellar remnants (double neutron stars or neutron star–black hole binaries; Paczynski 1991; Narayan et al. 1992). Both source candidates can create the central engine required to start the relativistic outflow.

The GRB prompt emission features a non-thermal spectrum that is, for the most part, well described by the phenomenological Band function, which is composed of two smoothly connected power laws peaking at  $\lesssim$  MeV energies (Band et al. 1993). However, in recent years, evidence has grown that two additional components may be present besides the Band function (e.g. Guiriec et al. 2015, and references therein): a thermal component, peaking typically at  $\sim 100$  keV, and a component at high energies ( $\gtrsim 100$  MeV) with a completely separate temporal evolution. The high-energy component has a delayed onset with respect to emission at lower energies and features a long-lived emission ( $\gtrsim 100$  s), which decays smoothly as  $\sim t^{-1}$  as a function of time  $t$  (Ackermann et al. 2013).

The Band function spectra are often attributed to the synchrotron emission of internal-shock accelerated electrons. The maximum photon energy of synchrotron emission is limited (e.g. Guetta & Granot 2003), but in so-called leptonic models, the internal shock could produce high-energy emission through synchrotron self-Compton (SSC) processes (e.g. Galli & Guetta 2008). Other internal-shock models, the so-called hadronic models, consider proton synchrotron emission (e.g. Razzaque et al. 2010) and/or the inverse Compton emission from secondary particles produced in internal cascades (Asano et al. 2009).

The GRB afterglow emission is attributed to the external shocks, and in the external-shock scenario they could also be the origin of the high-energy component. In the very bright GRB 130427A, several photons were found that appear to be incompatible with the model of synchrotron radiation emitted by electrons accelerated at the external forward shock (Ackermann et al. 2014). In leptonic scenarios, possible origins of the high-energy component are SSC emission in the forward shock (e.g. Sari & Esin 2001) or the reverse shock (e.g. Granot & Guetta 2003) or a combination of both (e.g. Fraija et al. 2016). Hadronic models also exist for the external-shock scenario (see e.g. Böttcher & Dermer 1998).

The observation and temporal evolution of GRB spectra at very-high energies (VHE;  $> 100$  GeV) can help distinguish between the myriad of models. For example, the detection of TeV photons at early times would be difficult to explain with internal SSC emission. Satellite experiments, like the Large Area Telescope on board the *Fermi* spacecraft (*Fermi*-LAT; Atwood et al. 2009), are limited in size and, since the photon flux decreases steeply with energy, only a few photons can be expected in the VHE regime. Imaging Atmospheric Cherenkov Telescopes (IACTs) are sensitive in this energy range and routinely look for TeV emission from GRBs, but only upper limits have been reported so far (Albert et al. 2007; Aharonian et al. 2009a; Acciari et al. 2011). One limitation for IACTs is that they are pointed instruments and thus need to slew the telescopes to the GRB position first. They are therefore not likely to observe long GRBs during their prompt phase, but will mostly observe in the afterglow phase (an exception to this can be found in Aharonian et al. 2009b). Observational constraints lead to a  $\sim 10\%$  duty cycle, and the Cherenkov Telescope Array (CTA), the next-generation IACT array, is expected to detect of the order of a few GRBs per year (Inoue et al. 2013).

The other ground-based technique uses extensive air shower (EAS) arrays that feature a large field of view ( $\sim 2$  sr or 16% of the sky) and near 100% duty cycle.

They are less sensitive to transient sources than IACTs, but the lack of observational delays allows them to observe the prompt phase of long and short GRBs. The High Altitude Water Cherenkov (HAWC) Observatory is a new EAS array (see next section). HAWC is mostly sensitive to short GRBs and can detect as many as 1 to 2 GRBs per year (Taboada & Gilmore 2014). However, this study used a sensitivity at low energies that has not been achieved yet. In this paper, the results of the analysis of GRB data with the current best analysis from the first 18 months of full operation of HAWC are reported.

## 2. THE HAWC GAMMA-RAY OBSERVATORY

HAWC is located at Sierra Negra, Mexico, at an altitude of 4,100 m above sea level (Abeysekara et al. 2017). It employs the water Cherenkov technique, in which VHE photons are detected by measuring Cherenkov light from secondary particles created in the EAS. HAWC comprises of 300 steel tanks containing light-proof bladders of 7.3 m diameter and 4.5 m depth, each holding  $\sim 200,000$  litres of filtered water. Each tank is instrumented with three 8" photomultiplier tubes (PMTs) and one 10" PMT on the bottom. Cables connect the PMTs to a central counting house, where the PMT pulses are shaped and discriminated at two thresholds.

HAWC features two systems for data acquisition (DAQ). The main DAQ measures the arrival time and time over threshold (TOT) of PMT pulses. The TOT is characteristic of the PMT's measurement of the charge (and hence the amount of Cherenkov light in the tank) and the information from different tanks allows the reconstruction of the EAS core. The core and the signal arrival time in different tanks permit the reconstruction of the direction of the incident shower. The scaler DAQ counts each PMT signal that exceeds the lower discrimination threshold in 100 ms windows. GRBs are detected by a statistically significant excess of counts over the noise rate ("single particle technique"; Vernetto 2000). The scaler DAQ is sensitive to showers of lower energies that cannot be reliably reconstructed with the main DAQ. These different energy sensitivities make the DAQs complement each other (Abeysekara et al. 2012). In this paper, data from the main DAQ are analysed.

HAWC uses a software trigger. All PMT signals are kept in memory and an EAS event is formed if a certain threshold on the number of coincident signals in a 150 ns time window is met (trigger threshold). The overwhelming majority of events recorded by HAWC originate from hadronic cosmic rays. The lateral charge distribution on the ground can help to determine the species of the

primary particle and a set of cuts, called the gamma-hadron (GH) separation cuts (see further information in the next section), can be used to obtain a purer gamma-ray event sample.

Construction of the HAWC Observatory began in 2012. During the early construction phase, when 29 tanks with 115 deployed PMTs were operational (HAWC-30), HAWC provided the first limits on the prompt VHE emission of GRB 130427A, the most powerful burst ever detected with a redshift  $z \lesssim 0.5$  (Abeysekara et al. 2015). The small detector and large zenith angle of the GRB caused the limits to be about two orders of magnitude higher than a simple extrapolation of the *Fermi* data.

Science operations of the HAWC array started with a partially built array (called HAWC-111) in August 2013. A search for VHE emission from 18 *Swift*-detected GRBs that occurred in the HAWC field of view between 2013 August 2 and 2014 July 8 showed that none of the GRBs is significant above  $3\sigma$  after accounting for trial factors (Lennarz & Taboada 2016).

Data taking with 250 tanks began on 2014 November 26 and even though the array was still gradually growing, this data set is regarded as full HAWC data. In this paper, GRBs observed up to 2016 June 29 are covered. During this period, detector uptime was about 92%, with downtime mainly caused by power failures and scheduled construction and maintenance (Abeysekara et al. 2017). During the time from HAWC-111 to the beginning of the full operation of HAWC, three bursts detected by *Fermi*-LAT, one burst detected by *Swift* and one burst triangulated by the Interplanetary Network (IPN) were in the HAWC field of view, but none of the GRBs was significant above  $2\sigma$  (Lennarz et al. 2017).

HAWC has an extensive GRB programme. An automated analysis is triggered at the HAWC site, if a GRB reported by satellites through the GRB Coordinates Network<sup>1</sup> (GCN) is within the HAWC field of view (for zenith angles smaller than  $45^\circ$ ). Results are available within  $\sim 30$  minutes. The analysis can also be redone if more accurate information becomes available later. HAWC reported the result of the analysis of GRB 160509A, a very bright burst detected by *Fermi*-LAT, but at a very high zenith angle of  $62^\circ$  at the HAWC site, within two days after the burst (Lennarz & Taboada 2016). HAWC also runs an untriggered search of the entire overhead sky (for more information, see Lennarz et al. 2017).

<sup>1</sup> <http://gcnc.gsfc.nasa.gov>

In addition to the analysis at the HAWC site, GRBs are also analysed off-site. This allows the use of improved calibration, event reconstruction and analysis methods, and all the available information on a certain GRB. In this paper, results from the off-site GRB analysis are shown.

### 3. ANALYSIS METHOD

HAWC classifies events into 10 size bins (zero to nine) based on the fraction of the PMTs that participate in the event. This method yields more stable results than cutting on the absolute number of PMTs in an event, as it compensates for detector changes, such as in the final stages of construction. The current trigger threshold of HAWC allows for events below the lowest size bin (here called threshold events). Events in higher size bins correspond on average to higher energy primary particles and have a better point spread function (PSF) and a better GH separation.

The analysis presented here is based on HAWC observations of the Crab Nebula (Abeysekara et al. 2017). GH separation cuts were found by optimising the statistical significance of the Crab using about 60% of the data set. In size bins 1 to 9, the cut variables are, within systematic uncertainties, well modelled using Monte Carlo simulations of gamma- and cosmic-ray air showers and a detailed simulation of the detector. There is a discrepancy in size bin 0 and, at the current time, no reliable set of GH separation cuts is available for this bin. This is why the events in bin 0 and the threshold events were excluded from the Crab analysis. Details on the sensitivity, cuts, background rejection and systematic uncertainties can be found in Abeysekara et al. (2017).

The Crab analysis uses a binned-likelihood method, but here a classical ON/OFF method (for example used in the Whipple observatory; Weekes et al. 1989) is employed. In short, it consists of defining a search circle around the position of the GRB, determining an estimated number of background events that will appear in it and finally calculating the number of events above background in the search circle. The  $p$ -value, which is the probability of obtaining equal or more counts from the background than the ones in the search circle, is calculated assuming a Poisson distribution with the estimated background as the mean.

#### 3.1. Event Selection

In this paper, only a single analysis bin is used, combining size bins 1 to 9 with the GH separation cuts corresponding to size bin 1 of the Crab analysis. VHE photons are attenuated due to interactions with the extragalactic background light (EBL), so most of the signal

from a GRB is expected at low energies. Hence, the expected signal is dominated by the lowest bin, so the gain from a multi-bin analysis with separate GH separation cuts for each bin is expected to be small. In previous analyses, the events were selected by combining size bins 0 to 9 plus the threshold events and applying no GH separation cuts (Lennarz et al. 2017).

The efficiency of the event selections can be compared for exceptional, historic GRBs at different redshifts. EBL absorption is assumed according to the fiducial model in Gilmore et al. (2012). For a nearby burst like GRB 130427A ( $z = 0.34$ ), where the high-energy component followed a power law with index  $-1.66$  (Ackermann et al. 2014), the analysis starting at bin 1 with GH separation cuts nearly doubles the expected significance compared to an analysis using bins 0–9 and no GH separation cuts. For a short burst like GRB 090510 at a redshift of 0.903 and a high-energy component proportional to  $E^{-1.54}$  (Ackermann et al. 2010), the two event selections result in a similar significance. At higher redshifts, e.g. GRB 090902B at a redshift of 1.8 and a high-energy component proportional to  $E^{-1.59}$  (Abdo et al. 2009), an analysis including size bin 0 and no GH separation cuts would perform better, but the detection would be marginal even if the burst occurred right at zenith. Hence, the analysis starting with bin 1 with GH separation cuts performs better than or equal to the event selection previously used.

Size bin 1 in the Crab analysis has a peak energy of  $\sim 550$  GeV. For GRB 130427A, the peak energy shifts to  $\sim 300$  GeV, showing that the relationship between the size bin number and the energies of the primary particles it includes depends on the gamma-ray spectrum. The difference arises from the fact that EBL absorption removes photons at higher energies. Below  $\sim 1$  TeV, HAWC can only detect photons if they interact deep in the atmosphere, allowing particles to still reach the detection level. Deeply interacting low-energy photons can have the same event size as a primary gamma ray of higher energy. Since the detector response has been characterized in terms of size bins, the uncertainties derived from the Crab analysis still apply here, even if the energy spectrum is different.

#### 3.2. Search Circle and Search Duration

The Crab analysis has demonstrated that the HAWC PSF in size bins 1 to 9 is, within systematic uncertainties, well described by the Monte Carlo simulations and thus the size of the search circle in the current analysis can also be optimised using simulations of gamma-ray air showers at different zenith angles. As the redshift increases, the GRB signal is increasingly domi-



nated by gamma rays of lower energy with worse angular resolution, so the optimal search circle increases. For the exceptional, historic GRBs mentioned above, for GRB 130427A ( $z = 0.34$ ), a search circle of  $0.8^\circ$  is optimal, while for GRB 090510 ( $z = 0.903$ ) and GRB 090902B ( $z = 1.8$ ), the optimal search circle is  $1.0^\circ$ . For GRB 130427A, a  $1.0^\circ$  search circle performs only marginally worse ( $< 10\%$ ), and since the redshift remains unknown for most GRBs, the angular bin is conservatively chosen to be  $1.0^\circ$ . The optimal search circle does not depend strongly on the zenith angle of the GRB.

In the ON/OFF method, the search circle follows the GRB position for a certain amount of time called the search duration. One search duration used in this paper is the GRB  $T_{90}$  derived from observations at lower energies. However, due to the delayed onset and long-lived emission of the high-energy component seen by *Fermi*, this timescale is not necessarily optimal for HAWC. Thus, for long GRBs, the search duration is expanded to  $3 \times T_{90}$  and  $10 \times T_{90}$ . For short GRBs, even  $10 \times T_{90}$  might search a very similar time scale to  $T_{90}$ , so instead 6 s ( $= 3 \times 2$  s) and 20 s ( $= 10 \times 2$  s) are searched.

### 3.3. All-sky Event Rate

HAWC records data at a rate of about 23 kHz using the current trigger threshold. Restricting the analysis to the single analysis bin discussed earlier (combining size bins 1 to 9 and applying the GH separation cuts for size bin 1) reduces the rate to about 700 Hz. Figure 1 shows the rate around the time of GRB 151205A. The all-sky event rate is well described by a constant plus a sinusoidal oscillation with a 12 hr period. The sinusoidal variation, of the order of  $\sim 0.8\%$ , is caused by atmospheric tides that affect the air shower propagation. The magnitude of this effect is very stable in three years of HAWC data. The sinusoidal is well fit with as little as  $\sim 70$  minutes of data used, but fails if only one hour of data is used.

The all-sky event rate serves as a tool to assess the data quality. Problems with the detector can result in sudden changes in the rate, which would show up as an unusually high fitted value for the sinusoidal variation. The fit of the all-sky event rate is also used as a way to estimate the expected number of background in the search circle.

### 3.4. Background Estimate

The ON/OFF method estimates the background in the search circle using off-observations like the ones shown in Figure 2. At time zero, the search circle is centred on the GRB position and follows it for the

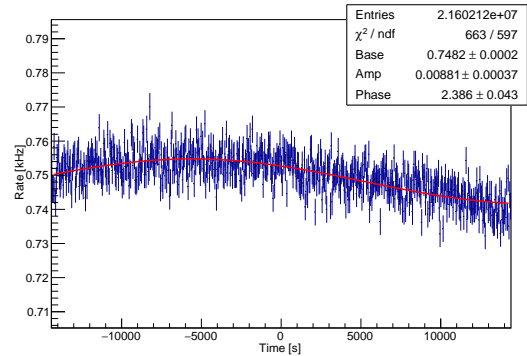


**Figure 1.** All-sky event rate in bins of width  $T_{90} = 48.0$  s around the trigger time of GRB 151228B at time zero as a representative example. The data are well fitted by a constant (base) plus a sinusoidal modulation. The fitted amplitude is relative to the constant.

search duration (on-observation). For the other times, the search circle is offset in right ascension by multiples of the search duration (off-observations), thus observing an empty field of the sky that covers the same zenith angles as the on-observation but at a different time. Off-observations are available before and after the GRB, thanks to the continuous data taking of HAWC. For short search durations, the off-observations can spatially overlap. Hence, an off-observation is only taken into account if it has a temporal offset of at least 480 s (corresponding to an angular offset of  $\sim 2.0^\circ$ ) to the previous one. The observations between  $\pm 600$  s are not used in order to avoid contamination in the off-observations due to the size of the HAWC PSF. The time implies that the closest off-observations have an angular offset of  $\sim 2.5^\circ$  from the on-observation, and even at the worst observation conditions, the contamination is less than 5%.

A background estimate at each point can be obtained using three different methods. In the first method, the off-observations are averaged. The average ignores the sinusoidal variation seen in Fig. 1, so in the second method, the fit of the all-sky event rate is scaled to match the summed counts in Fig. 2 (again avoiding overlapping off-observations). The resulting line in Fig. 2 is almost indistinguishable from a constant, showing that the sinusoidal oscillation is a negligible correction in a  $1^\circ$  search circle.

The third method exploits the fact that HAWC is a counting experiment and thus the distribution of counts in the off-observations (again excluding overlapping ones) should follow a Poisson distribution. An independent estimate for the expected background counts in the on-observation can be obtained from the mean of a Poisson distribution fitted to the count distribution (Fig. 3). The good fit to a Poisson distribution shows

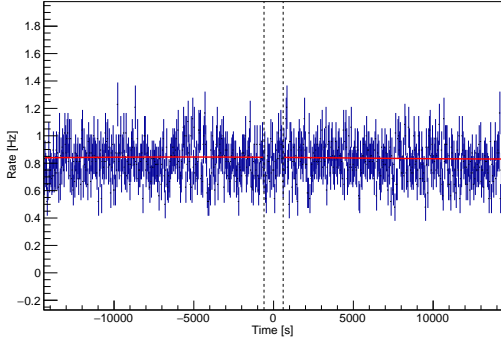


**Figure 2.** Event rate in bins of width  $T_{90} = 48.0$  s for the on-observation (at zero) and off-observations before and after the trigger time of GRB 151228B (zenith angle  $\sim 11^\circ$ ). The red line shows the background model that is created by scaling the all-sky event rate fit from Fig. 1. The vertical dashed lines show the region where data are not used for the scaling of the background model.

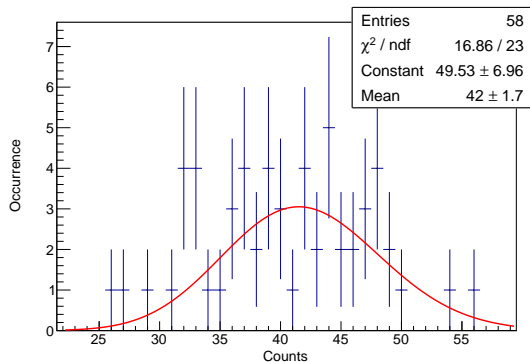


**Figure 3.** Histogram of the counts in the non-overlapping off-observations before and after the trigger time of GRB 151228B from Fig. 2. The distribution is well fitted by a Poisson distribution with mean  $\sim 42$ .

that there is no evidence for correlations between counts that would create a problem for the analysis.

All three methods yield consistent results for all GRBs, short and long, and independent of the burst zenith angle. The successful fit of the Poisson distribution also shows that it is adequate to calculate the significance assuming a Poisson distribution. The default method used is the scaled all-sky event rate. If the all-sky event rate is not available due to insufficient data around the GRB time, the background estimate is obtained using the mean of the off-observations. The background estimate is only deemed reliable if at least 10 independent off-observations are used.

### 3.5. Poorly Localised GRBs

The GRBs detected by the Gamma-ray Burst Monitor on board the *Fermi* satellite (*Fermi*-GBM; Meegan

et al. 2009) typically have a positional uncertainty that is wider than the HAWC optimal search circle. In this case, a circle defined by the error radius given by *Fermi*-GBM is covered by multiple search circles, where each circle is offset by  $0.3^\circ$  in right ascension or declination until the whole region of interest is covered. The *Fermi*-GBM error radius is the statistical  $1\sigma$  error, but since the errors are not symmetric, the given value is the average of the error ellipse. In the online *Fermi*-GBM Burst Catalog, only the average error radius is available. In addition to the statistical error, *Fermi*-GBM has a systematic uncertainty that is well represented (68% confidence level) by a  $3.7^\circ$  Gaussian with a non-Gaussian tail that contains about 10% of GBM-detected GRBs and extends to approximately  $14^\circ$  (Connaughton et al. 2015). Limiting the search to the 68% statistical error implies that occasionally the actual GRB position will not be inside the region of interest. For GRBs close to the edge of the HAWC field of view, it is possible that the error radius extends beyond the HAWC field of view. In those cases, the whole region of interest cannot be covered.

The significance reported here is the highest significance of all search circles. However, this procedure introduces a trial factor. A post-trial significance is derived by using the off-observations. For each off-observation, the most significant result of all search circles is taken and thus a distribution of pre-trial significances is built. The post-trial significance is then obtained by comparing the significance of the on-observation to that distribution. The off-observations are also allowed to overlap in time to increase the statistics of the pre-trial significance distribution.

## 4. RESULTS

During the first one and a half years of HAWC operations with the full HAWC detector, HAWC took data for 72 of 76 GRBs in its field of view, demonstrating the excellent uptime fraction of the detector. The data for nine bursts cannot be analysed due to issues with the data. All of these problems occurred in 2015, while all of the bursts in 2016 can be analysed, since the data taking became more stable. The GRBs analysed and the data used for the analysis are listed in the Appendix (Tables 7–9).

Four GRBs detected by *Fermi*-LAT were inside the HAWC field of view (160503A, 160310A, 150416A and 150314A). Due to power issues, GRB 160503A was missed and thus cannot be analysed. GRB 150416A was only located by *Fermi*-GBM, so it is treated like a GBM burst in the analysis. GRB 150314A, which also triggered *Swift*, occurred at a time when data taking

with HAWC was unstable. The analysis would require a different approach, and given the fact that the burst was located at the edge of the HAWC field of view ( $47^\circ$ ), the data were instead inspected by eye and nothing interesting was seen.

In addition to GRB 150314A, 21 *Swift* bursts were inside the HAWC field of view. The detector rate was unstable when GRB 150910A occurred, so these data are not suited for the analysis procedure described earlier. GRB 150323A occurred at a time when data taking with HAWC was unstable, so there is not enough data available to reach 10 independent off-observations. An inspection by eye reveals no outstanding signal, which is not surprising given that these bursts have the two longest  $T_{90}$  in the sample and HAWC is not very sensitive to long bursts. The prompt phase of GRB 160624A was not observed by HAWC due to problems with the detector.

During the same time period, *Fermi*-GBM has detected 64 GRBs that were inside the HAWC field of view, which includes the four detections by *Fermi*-LAT mentioned above and nine co-detections with *Swift* (in addition to GRB 150314A), which leaves 51 GRBs observed only by *Fermi*-GBM. For bn 160609690 and bn 150520893, no HAWC data are available. The data for bn 151211672, bn 150911315, bn 150819440, bn 150612702, bn 150528656 and bn 150208929 show instability in the trigger rate, and these bursts are thus not analysed.

GRB 170206A is the third brightest short GRB detected by *Fermi*-GBM so far and occurred during the writing of this paper. The low zenith angle of  $11^\circ$  and the fact that the burst was also detected by *Fermi*-LAT (Fana Dirirsa et al. 2017) make this burst an excellent candidate for HAWC. The burst is included in this paper using data reconstructed directly at the HAWC site. Differences from the current offline analysis are only minor.

Table 1 and Table 2 show the results for the analysis using the low energy  $T_{90}$ . Table 3–6 show the results for the extended time periods. All GRBs are consistent with the assumption of background only. Event upper limits are derived as the upper edge of frequentist confidence intervals (Patrignani et al. 2016). A likelihood-ratio ordering principle first described by Feldman & Cousins (1998) is used. The upper limits are converted to a flux limit using the HAWC effective area derived from the Monte Carlo described in Abeysekara et al. (2017). Flux limits are given for a power-law spectrum with an index of  $-2.0$ , which is the average value for the photon index of the high-energy component measured by *Fermi*-LAT (Ackermann et al. 2013), and assuming EBL absorp-

tion according to the fiducial model in Gilmore et al. (2012). Short GRBs might have a somewhat harder index, as seen in GRB 081024B (Abdo et al. 2010) and GRB 090510 (see above). Assuming a photon index of  $-1.7$  would improve the limits by a factor of about 6 for a burst at a redshift of 0.3 at zenith and 7 for a burst at a zenith angle of  $40^\circ$ . For a burst at a redshift of 1.0, the limits would improve by a factor of 4.

The energy range of these limits, described by the energy range that gives the central 90% of the total number of expected counts, depends on the zenith angle and redshift of the burst. For a burst with a power-law spectrum with index  $-2$  at a redshift of 0.3, the range is about 100 GeV to 1 TeV at zenith and increases to about 150 GeV to 3 TeV at a zenith angle of  $40^\circ$ . If the burst is at a redshift of 1.0, EBL absorption removes most of the expected counts at higher energies, making the 90% range very narrow. The lower bound changes from 50 to 70 GeV when going from zenith to a zenith angle of  $40^\circ$ , while the upper end of the 90% range ends at about 200 GeV. This shows again that the relationship between the size bin number and the energies of the primary particles it includes depends on the gamma-ray spectrum.

## 5. DISCUSSION AND OUTLOOK

The two short GRBs 080825C and 090501 had ratios of high-energy (100 MeV–10 GeV) to low-energy (10 keV–1 MeV) fluences over 100% (Ackermann et al. 2013). Figure 4 compares the *Fermi*-GBM fluence with the fluence implied by the HAWC upper limits for all GRB with an error radius that does not extend beyond the HAWC field of view. As expected, the fluence limits deteriorate when going to higher redshifts, since due to EBL absorption less signal is expected from a GRB. For all short GRBs that occurred during the first 18 months of HAWC data taking with the full HAWC detector, the HAWC fluence limits are above the fluence measured by *Fermi*-GBM. For long GRBs, there are several GRBs (bn160215773, bn160113398, bn151030999, bn150126868) where the HAWC fluence limit is below the fluence measured by *Fermi*-GBM if the GRB is as close as  $z = 0.3$ . However, only about 20% of long GRBs are closer than  $z = 1.0$ , so the number of long GRBs at a redshift of 0.3 or closer should be fairly low.

GRB 170206A is the only GRB where the fluence implied by the HAWC upper limits in the HAWC energy range is below the *Fermi*-GBM fluence in the GBM energy range for both a redshift of 0.3 and 1, which is why this burst is the most interesting so far. Up to 2017 February, *Swift* has detected 22 short GRBs that have a redshift measurement available, and only four



**Table 1.** Results for *Fermi*-LAT- and *Swift*-detected GRBs

	Measure- ment	Background Estimate	Signif- icance	Upper Limit	Sensi- tivity	$A$ at 1 GeV <sup>a</sup> $z = 0.3$	$A$ at 1 GeV <sup>a</sup> $z = 1.0$	$A$ at 1 GeV <sup>a</sup> GRB $z$
170206A	0	0.90	...	1.67	3.19	6.05e-11	1.20e-09	...
160310A	5	4.46	0.10	5.53	4.98	1.92e-10	6.26e-09	...
160410A	2	2.49	-0.55	3.46	4.19	—	—	3.88e-08
151228B	36	40.45	-0.77	7.10	12.22	6.28e-12	1.25e-10	...
151205A	36	32.58	0.53	14.45	11.11	1.95e-11	4.26e-10	...
150817A	7	11.37	-1.52	2.55	7.06	2.97e-11	9.60e-10	...
150811A	2	6.41	-2.25	1.36	5.66	2.53e-11	8.27e-10	...
150716A	5	5.94	-0.54	4.12	5.51	2.32e-10	1.02e-08	...
150710A	0	0.10	...	2.33	2.52	5.49e-10	8.52e-09	...
150530B	10	7.06	0.93	9.44	5.90	1.03e-10	2.91e-09	...
150530A	1	1.18	-0.50	3.19	3.40	7.19e-10	2.41e-08	...
150527A	20	12.74	1.80	15.75	7.41	3.49e-10	1.54e-08	...
150428A	1	2.60	-1.44	2.12	4.24	8.12e-10	1.97e-08	...
150423A	0	0.12	...	2.31	2.54	5.09e-10	9.33e-09	2.85e-08
150323B	9	11.96	-1.00	3.95	7.23	6.50e-11	1.57e-09	...
150317A	4	4.29	-0.31	4.30	4.92	1.82e-10	4.40e-09	...
150302A	13	8.39	1.38	11.67	6.29	1.52e-10	4.12e-09	...
150211A	1	1.09	-0.42	3.27	3.34	1.90e-09	7.38e-08	...
150203A	15	21.88	-1.64	2.75	9.35	5.16e-12	9.45e-11	...
141205A	2	0.74	0.95	5.17	3.06	3.38e-10	7.64e-09	...

NOTE—Results for *Fermi*-LAT-detected bursts 170206A and 160310A and the 18 *Swift*-detected GRBs in the HAWC field of view that are analysed in this paper. The *Fermi*-LAT-detected burst GRB 150416A can be found in Table 2. For each GRB, the measurement and the corresponding background estimate from the data are given (in units of counts). The corresponding  $p$ -value from a Poisson distribution is converted to the standard deviation of a Gaussian distribution (significance), except when the measurement is zero, which means the  $p$ -value is 1, and an equivalent standard deviation is undefined. The event upper limits correspond to a 90% confidence level and sensitivity is the corresponding average event upper limit as defined in [Feldman & Cousins \(1998\)](#). Flux limits are given for a power law  $A \left( \frac{E}{1 \text{ GeV}} \right)^{-2.0}$  assuming redshifts of 0.3, 1.0 or the GRB redshift if known. See the main text for the validity range of the limits. The redshift for 150423A is only tentative, so all three options are given.

<sup>a</sup>(cm<sup>-2</sup>s<sup>-1</sup>keV<sup>-1</sup>)

of them were at a redshift larger than 1, so it is likely that GRB 170206A was at a redshift below 1. Taking the ratio implies that GRB 170206A had less than 3% (50%) of the fluence in the *Fermi*-GBM energy range in the HAWC energy range for a burst at a redshift of 0.3 (1.0). If the GRB spectrum was cut off at 100 GeV, the ratio between HAWC and GBM would change to 63% (130%) for a burst at a redshift of 0.3 (1.0). A high-energy cut-off can be expected in SSC prompt emission models due to pair production. Figure 5 compares the prompt spectrum measured by *Fermi*-GBM to “quasi-differential” limits that are calculated by restricting an

$E^{-2}$  spectrum to the energy ranges indicated by the limit bars.

Figure 5 also shows the best-fit spectrum from *Fermi*-LAT, obtained using the P8.TRANSIENT010E class of LAT data. Events were selected with energies between 100 MeV and 100 GeV and a zenith angle smaller than 90°, contained within a circular region centered on the GRB position with a radius of 12°. The GRB was 67° from the LAT boresight at the time of the trigger, at the edge of the LAT field of view, where the effective area is ~30% of the on-axis area. This suboptimal position resulted in only four detected photons in the 20 s following the trigger. The standard Fermi Science Tools

**Table 2.** Results for *Fermi*-GBM-detected GRBs

	Measure- ment	Background Estimate	Signif- icance	Post-Trial Signif.	R.A. (deg)	Decl. (deg)	Upper Limit	Sensi- tivity	A at 1 GeV <sup>a</sup> z = 0.3	A at 1 GeV <sup>a</sup> z = 1.0
bn160605847	4	0.97	2.11	-0.51	107.37	-18.1	7.62	3.25	1.37e-09	3.29e-08
bn160527080	9	3.70	2.21	-1.46	216.50	10.5	11.60	4.70	6.84e-10	2.29e-08
bn160521839	10	3.72	2.57	0.12	75.79	-14.0	12.78	4.71	5.08e-10	1.66e-08
bn160515819	22	14.47	1.76	-1.40	84.18	-16.0	16.50	7.82	1.93e-10	4.64e-09
bn160406503	3	0.26	2.81	-0.05	259.06	21.2	7.16	2.66	1.19e-09	2.70e-08
*bn160315739	3	0.21	3.01	-0.59	305.29	-8.2	7.21	2.62	1.72e-08	6.65e-07
*bn160303201	9	1.92	3.58	1.12	161.59	65.3	13.38	3.87	1.02e-08	1.34e-06
bn160301215	16	9.29	1.91	-0.92	113.11	2.3	14.71	6.56	1.53e-10	4.15e-09
*bn160228034	12	3.71	3.30	0.29	43.23	43.7	15.29	4.71	5.98e-10	1.95e-08
*bn160220868	23	10.69	3.18	-0.47	340.67	13.6	21.30	6.92	1.25e-10	3.13e-09
bn160215773	54	37.82	2.42	-0.12	354.60	0.0	29.65	11.85	9.47e-11	3.07e-09
bn160211119	2	0.08	2.71	1.19	117.06	56.1	5.83	2.51	2.85e-08	8.83e-07
bn160206430	11	4.32	2.58	0.17	181.41	53.8	13.48	4.93	6.19e-10	1.49e-08
bn160131174	165	132.24	2.72	-0.28	112.64	15.2	55.25	21.13	1.69e-11	3.56e-10
bn160118060	7	3.91	1.27	-0.37	19.17	59.9	8.62	4.78	8.64e-10	2.68e-08
bn160113398	13	9.33	1.04	-0.52	186.54	12.0	10.72	6.57	9.51e-11	2.69e-09
bn160107931	11	7.77	0.99	...	...	...	10.04	6.12	6.98e-10	2.70e-08
bn160102500	11	3.96	2.79	0.22	223.36	11.4	13.85	4.80	8.16e-10	2.73e-08
bn151129333	11	3.75	2.92	0.41	57.93	-12.6	14.06	4.72	2.13e-09	8.26e-08
bn151030999	91	86.27	0.47	...	...	...	21.75	17.33	9.03e-12	1.65e-10
*bn151023104	8	2.06	3.01	-0.43	349.84	-11.7	11.93	3.94	7.35e-10	2.40e-08
*bn151022577	2	0.10	2.61	-0.94	108.39	21.3	5.81	2.52	5.62e-09	1.52e-07
bn150928359	10	2.96	3.09	0.97	89.52	34.8	13.54	4.39	5.15e-09	1.25e-07
*bn150923297	1	0.02	2.09	-0.01	325.21	24.7	4.33	2.45	1.06e-07	3.29e-06
bn150906944	2	0.15	2.31	0.32	215.84	-1.7	5.75	2.57	1.83e-09	3.97e-08
*bn150904479	4	0.73	2.48	-2.00	74.39	-28.1	7.87	3.05	1.24e-08	1.63e-06
bn150811849	0	0.09	...	...	...	...	2.34	2.52	3.61e-09	8.70e-08
bn150721242	3	1.36	1.00	-0.51	333.12	7.5	6.06	3.53	2.60e-09	1.01e-07
bn150705588	2	0.16	2.26	-0.97	64.33	-3.6	5.75	2.58	5.15e-09	1.68e-07
bn150622393	2	4.12	-1.38	...	...	...	2.25	4.86	2.94e-10	1.14e-08
bn150522944	3	0.24	2.91	0.54	121.03	53.7	7.19	2.64	4.43e-09	1.45e-07
bn150502435	15	15.93	-0.32	...	...	...	6.60	8.14	9.02e-11	3.02e-09
bn150416773	8	3.28	2.07	0.48	60.98	51.8	10.71	4.53	1.51e-09	4.68e-08
*bn150329288	8	1.58	3.49	0.92	170.92	-21.4	12.41	3.67	3.40e-09	1.32e-07
*bn150318521	4	2.05	1.03	-1.39	271.40	-31.1	6.54	3.94	7.26e-09	4.96e-07
*bn150206407	5	0.55	3.46	1.73	212.41	57.1	9.44	2.89	8.66e-09	2.68e-07
*bn150201040	2	0.13	2.44	-0.57	11.13	15.9	5.78	2.55	7.12e-09	2.33e-07
bn150131951	7	1.41	3.22	1.44	57.64	22.0	11.12	3.56	2.03e-09	6.79e-08
bn150128791	19	8.38	3.06	1.12	269.04	27.5	19.12	6.28	1.05e-09	3.27e-08
bn150126868	31	28.53	0.40	...	...	...	12.95	10.46	6.06e-11	1.96e-09
bn150110433	4	5.33	-0.77	...	...	...	3.33	5.29	9.10e-10	2.21e-08
bn150105257	9	8.98	-0.10	...	...	...	6.32	6.47	2.13e-10	9.35e-09
bn141230142	14	6.34	2.53	0.15	58.98	0.7	15.16	5.63	1.11e-10	2.50e-09
bn141202470	1	0.12	1.23	0.04	145.94	63.1	4.24	2.54	2.50e-08	9.68e-07

NOTE—Same as Table 1, but for the 44 *Fermi*-GBM-detected GRBs in the HAWC field of view that are analysed in this paper.

An asterisk indicates a GRB with an error radius that extends beyond the HAWC field of view. An additional column shows the significance after accounting for trials and the right ascension / declination of the location of the tile. GRBs with an error radius smaller than the HAWC search circle size have no post-trial significance and are centered on the GRB location.

<sup>a</sup> (cm<sup>-2</sup>s<sup>-1</sup>keV<sup>-1</sup>)

**Table 3.** Results for *Fermi*- and *Swift*-detected GRBs (Extended Time Search I)

	Measure- ment	Background Estimate	Signif- icance	Upper Limit	Sensi- tivity	$A$ at 1 GeV <sup>a</sup> $z = 0.3$	$A$ at 1 GeV <sup>a</sup> $z = 1.0$	$A$ at 1 GeV <sup>a</sup> GRB $z$
170206A	5	3.82	0.42	6.17	4.75	4.36e-11	8.66e-10	...
160310A	16	13.87	0.47	10.10	7.68	1.17e-10	3.82e-09	...
160410A	9	6.84	0.67	8.46	5.83	...	...	3.16e-08
151228B	102	117.05	-1.46	6.70	19.96	1.97e-12	3.92e-11	...
151205A	107	95.83	1.09	29.20	18.16	1.32e-11	2.87e-10	...
150817A	27	33.69	-1.26	4.55	11.25	1.76e-11	5.71e-10	...
150811A	12	22.40	-2.50	1.80	9.45	1.11e-11	3.63e-10	...
150716A	20	17.46	0.52	11.05	8.49	2.08e-10	9.14e-09	...
150710A	8	6.25	0.55	7.74	5.61	4.55e-11	7.05e-10	...
150530B	29	23.04	1.13	15.95	9.59	5.79e-11	1.64e-09	...
150530A	2	3.32	-1.01	2.79	4.54	2.10e-10	7.04e-09	...
150527A	47	40.72	0.91	18.80	12.25	1.39e-10	6.11e-09	...
150428A	7	7.89	-0.45	4.68	6.15	5.96e-10	1.45e-08	...
150423A	1	4.87	-2.42	1.26	5.13	1.01e-11	1.85e-10	5.67e-10
150323B	35	36.40	-0.29	9.65	11.67	5.29e-11	1.27e-09	...
150317A	11	13.43	-0.78	4.35	7.55	6.14e-11	1.48e-09	...
150302A	34	25.29	1.59	19.70	9.94	8.56e-11	2.32e-09	...
150211A	7	3.61	1.45	8.92	4.67	1.73e-09	6.71e-08	...
150203A	62	67.25	-0.69	9.30	15.40	5.81e-12	1.06e-10	...
141205A	6	4.09	0.74	7.38	4.85	8.84e-11	2.00e-09	...

NOTE—Same as Table 1, but using a search duration of three times  $T_{90}$  for long GRBs and six s for short GRBs.

<sup>a</sup>( $\text{cm}^{-2}\text{s}^{-1}\text{keV}^{-1}$ )

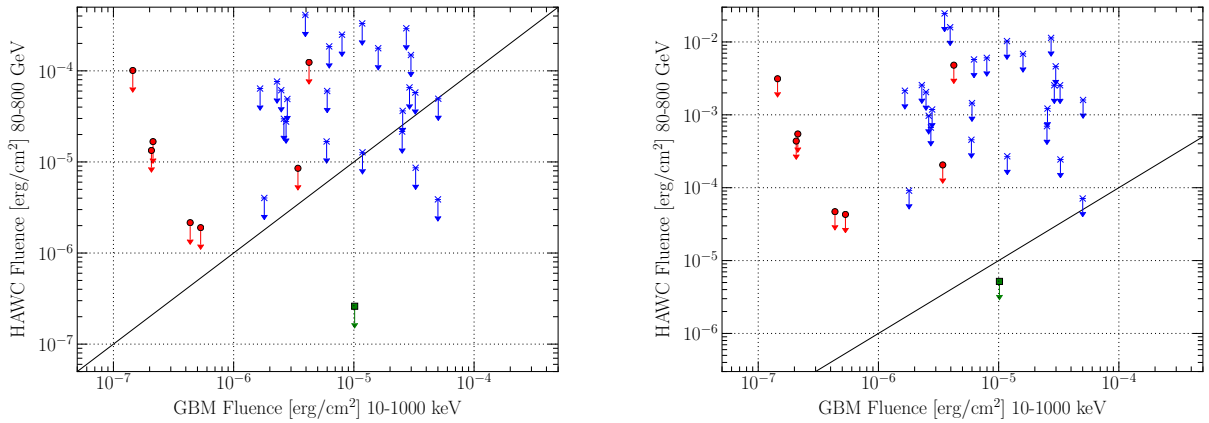


**Figure 4.** Comparison between the *Fermi*-GBM fluence and the fluence implied by the HAWC upper limits obtained during the same time period for all GRBs completely inside the HAWC field of view for the two different redshifts (left panel  $z = 0.3$ , right panel  $z = 1.0$ ). The circles (red) show short GRBs, the asterisks (blue) long GRBs, and the green square GRB 170206A. The black line shows an equal fluence in the *Fermi*-GBM and HAWC energy range.

**Table 4.** Results for *Fermi*- and *Swift*-detected GRBs (Extended Time Search II)

	Measure- ment	Background Estimate	Signif- icance	Upper Limit	Sensi- tivity	$A$ at 1 GeV <sup>a</sup> $z = 0.3$	$A$ at 1 GeV <sup>a</sup> $z = 1.0$	$A$ at 1 GeV <sup>a</sup> GRB $z$
170206A	12	13.77	-0.58	5.35	7.68	1.13e-11	2.25e-10	...
160310A	53	45.82	0.99	20.20	12.94	7.01e-11	2.29e-09	...
160410A	27	23.84	0.57	13.15	9.71	...	...	1.48e-08
151228B	392	389.71	0.10	35.50	35.12	3.14e-12	6.23e-11	...
151205A	338	333.61	0.22	35.50	32.53	4.80e-12	1.05e-10	...
150817A	114	107.06	0.63	25.45	19.12	2.96e-11	9.59e-10	...
150811A	71	76.80	-0.71	9.85	16.38	1.83e-11	5.97e-10	...
150710A	16	17.76	-0.51	6.35	8.56	1.12e-11	1.74e-10	...
150530B	83	77.07	0.63	21.95	16.42	2.39e-11	6.77e-10	...
150530A	10	10.11	-0.14	6.35	6.73	1.43e-10	4.80e-09	...
150527A	154	155.90	-0.18	19.50	22.66	4.32e-11	1.90e-09	...
150428A	20	28.26	-1.71	2.80	10.42	1.07e-10	2.60e-09	...
150423A	9	15.21	-1.83	2.35	8.01	5.68e-12	1.04e-10	3.19e-10
150323B	112	129.03	-1.57	6.35	20.90	1.04e-11	2.52e-10	...
150317A	31	42.01	-1.84	3.30	12.42	1.40e-11	3.37e-10	...
150302A	91	85.05	0.60	22.95	17.19	2.99e-11	8.10e-10	...
150211A	21	12.72	2.05	17.25	7.40	1.00e-09	3.89e-08	...
150203A	195	221.34	-1.83	6.50	26.78	1.22e-12	2.23e-11	...
141205A	12	13.14	-0.42	5.90	7.51	2.12e-11	4.80e-10	...

NOTE—Same as Table 1, but using a search duration of 10 times  $T_{90}$  for long GRBs and 20 s for short GRBs. There is not enough data for the analysis of GRB 150716A for this search duration.

<sup>a</sup> ( $\text{cm}^{-2}\text{s}^{-1}\text{keV}^{-1}$ )

v10r0p5 were used to perform an unbinned likelihood analysis with the tool *gtlike*. A likelihood model containing a source with a power-law spectrum (the GRB), as well as the Galactic and the Isotropic templates provided by the *Fermi*-LAT collaboration, were adopted. The normalization of the Galactic template was kept fixed. As customary for LAT analysis, the likelihood-ratio test (Neyman & Pearson 1928) was used to assess whether the GRB is detected or not. It uses as test statistic  $\text{TS} = 2(\log L_1 - \log L_0)$ , where  $L_1$  and  $L_0$  are the maximum of the likelihood for a model with and without the GRB, respectively. Monte Carlo simulations show that TS is distributed as  $1/2 \chi^2$  with 1 degree of freedom (Mattox et al. 1996).  $\text{TS} = 28$  was found for the GRB, corresponding to a significance of  $5.3\sigma$ . The best-fit photon index is  $-2.0 \pm 0.6$ , with an average flux (100 MeV–100 GeV) of  $(9 \pm 6) \times 10^{-4} \text{ ph cm}^{-2} \text{ s}^{-1}$ . HAWC limits can exclude a very hard photon index or require a spectral break in between the highest energy LAT photon (811 MeV) and the HAWC energy range for a nearby burst ( $z = 0.3$ ). For a GRB at a redshift

of  $z = 1.0$ , the HAWC limits are only marginally constraining.

GRB 160310A (Vianello et al. 2016) is the other well-located LAT GRB analysed in this paper, but the zenith angle of  $34^\circ$  is far from optimal for HAWC. Furthermore, this GRB is not detected in LAT data using the same selection and technique as used for GRB 170206A in the time intervals considered in this paper. It is detected on a much longer time scale (0–10 ks), as also reported in Vianello et al. (2016). Thus, in this case it is not possible to directly compare the HAWC upper limits to the LAT spectrum as was done for GRB 170206A.

The previous estimate of the GRB detection rate in HAWC used only triggers by *Fermi*-GBM, while in the current paper those GRBs as well as GRBs triggering *Swift* were analysed. *Swift* added about 15% uniquely identified bursts, so the GRB detection rate of HAWC should also be slightly higher. However, in Taboada & Gilmore (2014), a trigger threshold of 30 PMTs was used, which is significantly lower than the threshold of the current analysis (6.7% of PMTs participating in the



**Table 5.** Results for *Fermi*-GBM-detected GRBs (Extended Time Search I)

	Measure- ment	Background Estimate	Signif- icance	Post-Trial Signif.	R.A. (deg)	Decl. (deg)	Upper Limit	Sensi- tivity	$A$ at 1 GeV <sup>a</sup> $z = 0.3$	$A$ at 1 GeV <sup>a</sup> $z = 1.0$
bn160605847	8	3.35	2.03	-1.18	108.34	-16.6	10.64	4.56	6.36e-10	1.53e-08
bn160527080	20	9.50	2.88	0.05	214.43	1.8	19.02	6.61	6.21e-10	2.73e-08
bn160521839	25	12.70	2.97	0.68	73.62	-11.9	21.80	7.40	2.07e-10	6.69e-09
bn160515819	55	40.48	2.12	-0.46	82.64	-17.2	28.00	12.22	1.09e-10	2.63e-09
bn160406503	13	3.92	3.51	0.75	274.48	35.6	16.13	4.79	1.68e-10	3.56e-09
*bn160315739	5	0.50	3.58	0.60	304.04	-9.1	9.48	2.85	1.93e-08	4.69e-07
*bn160303201	23	9.64	3.57	0.85	153.10	63.2	22.27	6.65	1.22e-09	4.73e-08
bn160301215	42	28.97	2.21	-0.43	114.91	1.1	25.00	10.57	8.68e-11	2.35e-09
*bn160228034	24	11.09	3.28	0.06	43.23	43.7	22.40	7.02	2.92e-10	9.54e-09
*bn160220868	39	20.71	3.52	0.22	336.44	6.1	29.80	9.13	1.36e-10	3.70e-09
bn160215773	112	90.77	2.12	-0.95	360.00	2.7	39.75	17.72	9.25e-11	2.23e-09
bn160211119	3	0.55	2.10	-0.26	117.11	55.8	6.88	2.89	5.38e-09	1.67e-07
bn160206430	22	11.98	2.52	-0.09	180.85	54.4	19.00	7.24	2.91e-10	7.00e-09
bn160118060	17	12.03	1.27	-0.51	18.56	59.3	12.95	7.25	4.33e-10	1.34e-08
bn160113398	35	28.21	1.18	-0.42	186.54	12.0	17.80	10.41	5.26e-11	1.49e-09
bn160107931	27	21.21	1.14	...	...	...	15.75	9.21	3.65e-10	1.41e-08
bn160102500	26	13.52	2.94	0.28	221.83	10.5	22.00	7.58	2.86e-10	6.88e-09
bn151129333	22	11.15	2.79	0.05	57.93	-12.6	19.85	7.02	1.00e-09	3.89e-08
bn151030999	277	264.04	0.77	...	...	...	41.50	29.19	5.75e-12	1.05e-10
*bn151023104	15	5.73	3.12	-0.45	350.42	-12.6	16.79	5.43	5.39e-10	1.30e-08
*bn151022577	7	1.31	3.34	-0.34	107.20	38.4	11.21	3.49	1.18e-09	3.85e-08
bn150928359	22	9.62	3.34	1.24	88.76	34.2	21.36	6.64	2.71e-09	6.56e-08
*bn150923297	4	0.86	2.27	-0.69	329.09	30.1	7.74	3.16	1.93e-09	6.45e-08
bn150906944	11	3.77	2.91	0.61	214.35	5.5	14.04	4.73	1.68e-10	3.81e-09
*bn150904479	12	4.73	2.69	-1.59	70.55	-24.5	14.27	5.09	1.62e-09	6.26e-08
bn150811849	0	0.97	...	...	...	...	1.62	3.25	2.66e-10	6.42e-09
bn150721242	5	3.89	0.39	-1.80	333.73	7.5	6.10	4.77	8.74e-10	3.38e-08
bn150705588	8	2.33	2.77	-0.95	59.23	1.5	11.65	4.12	3.28e-10	7.90e-09
bn150622393	10	12.53	-0.85	...	...	...	4.25	7.36	1.85e-10	7.16e-09
bn150522944	7	1.13	3.57	1.28	139.71	53.4	11.39	3.37	1.87e-09	4.52e-08
bn150502435	45	44.57	0.02	...	...	...	12.50	12.77	5.69e-11	1.91e-09
bn150416773	20	10.11	2.66	0.97	59.54	52.4	18.40	6.73	8.66e-10	2.68e-08
*bn150329288	24	11.64	3.09	-0.31	166.24	-10.0	21.85	7.14	3.76e-10	1.26e-08
*bn150318521	9	6.24	0.92	-1.61	271.40	-31.1	9.05	5.61	3.35e-09	2.29e-07
*bn150206407	10	2.10	3.81	2.14	208.73	56.5	14.39	3.97	2.33e-09	1.02e-07
*bn150201040	7	1.61	2.99	-0.45	11.78	16.8	10.92	3.69	1.15e-09	3.75e-08
bn150131951	10	3.20	2.91	0.67	60.52	24.1	13.29	4.50	1.34e-09	5.91e-08
bn150128791	66	41.33	3.49	2.36	273.76	26.6	39.20	12.32	2.29e-10	7.67e-09
bn150126868	90	87.85	0.19	...	...	...	19.15	17.44	2.99e-11	9.67e-10
bn150110433	19	17.65	0.24	...	...	...	9.85	8.55	8.99e-10	2.18e-08
bn150105257	24	24.72	-0.21	...	...	...	8.75	9.85	9.82e-11	4.32e-09
bn141230142	36	20.10	3.13	1.04	53.88	0.7	26.90	9.01	6.54e-11	1.48e-09
bn141202470	3	0.77	1.72	-0.57	142.28	60.1	6.66	3.08	2.75e-09	1.21e-07

NOTE—Same as Table 2, but using a search duration of three times  $T_{90}$  for long GRBs and six s for short GRBs. There is not enough data for the analysis of bn160131174 for this search duration.

<sup>a</sup> ( $\text{cm}^{-2}\text{s}^{-1}\text{keV}^{-1}$ )

**Table 6.** Results for *Fermi*-GBM-detected GRBs (Extended Time Search II)

	Measure- ment	Background Estimate	Signif- icance	Post-Trial Signif.	R.A. (deg)	Decl. (deg)	Upper Limit	Sensi- tivity	$A$ at 1 GeV <sup>a</sup> $z = 0.3$	$A$ at 1 GeV <sup>a</sup> $z = 1.0$
bn160605847	25	11.22	3.46	1.72	108.34	-16.6	23.25	7.03	4.17e-10	1.00e-08
bn160527080	57	37.29	2.95	-0.09	213.82	3.3	33.20	11.77	1.96e-10	6.55e-09
bn160521839	42	23.36	3.41	1.46	72.07	-17.6	30.65	9.63	2.88e-10	9.66e-09
bn160406503	27	13.45	3.18	-0.33	274.02	35.0	23.55	7.57	7.38e-11	1.56e-09
*bn160315739	27	11.61	3.78	0.86	331.34	-7.9	25.35	7.16	1.66e-10	4.70e-09
*bn160303201	57	32.58	3.82	1.50	153.77	63.2	37.95	11.10	6.25e-10	2.42e-08
bn160301215	134	105.15	2.67	0.43	117.01	1.4	48.85	18.98	3.59e-11	1.01e-09
*bn160228034	91	58.18	3.93	1.36	46.80	37.4	49.80	14.41	6.73e-11	1.90e-09
*bn160220868	93	63.14	3.47	0.25	335.53	5.8	46.85	14.95	6.43e-11	1.74e-09
bn160215773	459	413.67	2.17	-1.25	357.00	1.5	81.50	36.15	3.64e-11	1.19e-09
bn160211119	7	2.12	2.50	0.00	115.69	54.9	10.40	3.98	2.44e-09	7.57e-08
bn160206430	62	37.81	3.55	1.36	184.99	55.9	38.20	11.85	1.75e-10	4.22e-09
bn160118060	47	37.23	1.49	-0.25	18.57	59.9	22.25	11.76	2.23e-10	6.91e-09
bn160113398	106	87.82	1.85	0.52	187.77	11.1	36.20	17.44	3.21e-11	9.09e-10
bn160107931	53	56.23	-0.48	...	...	...	10.00	14.22	6.95e-11	2.69e-09
bn160102500	83	55.78	3.36	1.15	218.82	7.5	43.25	14.17	1.08e-10	3.52e-09
bn151129333	100	72.76	2.99	0.46	66.53	-12.0	44.75	15.97	1.28e-10	4.29e-09
bn151030999	862	877.21	-0.53	...	...	...	35.50	52.26	1.47e-12	2.70e-11
*bn151023104	11	2.91	3.50	0.35	13.04	-10.2	14.89	4.38	1.53e-08	1.04e-06
*bn151022577	14	4.67	3.38	-0.54	104.22	21.0	16.83	5.07	5.31e-10	1.73e-08
bn150928359	98	73.63	2.67	-0.10	81.88	33.6	41.90	16.06	1.94e-10	8.55e-09
*bn150923297	7	1.48	3.14	0.62	323.04	27.4	11.05	3.61	4.38e-09	1.70e-07
bn150906944	18	9.79	2.26	-1.11	215.54	-1.1	16.37	6.68	8.31e-11	1.81e-09
*bn150904479	57	35.44	3.28	0.09	57.69	-19.7	35.05	11.52	2.25e-10	7.53e-09
bn150811849	0	3.26	...	...	...	...	0.84	4.52	4.14e-11	9.99e-10
bn150721242	21	12.75	2.03	0.62	333.73	6.6	17.20	7.41	7.39e-10	2.86e-08
bn150705588	13	4.68	3.05	-0.56	57.93	-8.7	15.38	5.07	4.85e-10	1.58e-08
bn150622393	36	37.37	-0.28	...	...	...	9.70	11.79	1.27e-10	4.91e-09
bn150522944	15	5.63	3.17	0.14	120.60	51.3	16.89	5.39	3.81e-10	1.23e-08
bn150502435	131	133.06	-0.21	...	...	...	18.00	21.19	2.46e-11	8.24e-10
bn150416773	44	33.35	1.71	-0.39	58.54	53.3	22.65	11.21	3.20e-10	9.91e-09
*bn150329288	64	38.48	3.71	0.89	166.54	-9.7	40.00	11.93	2.07e-10	6.92e-09
*bn150318521	33	23.29	1.83	-0.33	271.73	-30.5	20.20	9.62	7.85e-10	1.03e-07
*bn150206407	16	7.05	2.80	-0.02	208.73	56.5	16.95	5.89	8.22e-10	3.61e-08
*bn150201040	16	6.45	3.07	-0.60	13.54	21.0	17.54	5.67	3.96e-10	1.28e-08
bn150131951	24	13.69	2.45	-0.66	57.79	16.9	19.80	7.66	3.61e-10	1.21e-08
bn150128791	128	103.38	2.30	-0.62	272.42	26.0	44.60	18.86	7.81e-11	2.62e-09
bn150126868	307	293.39	0.77	...	...	...	43.50	30.75	2.03e-11	6.59e-10
bn150110433	70	68.29	0.17	...	...	...	16.70	15.51	4.57e-10	1.11e-08
bn150105257	100	91.54	0.84	...	...	...	26.00	17.81	8.76e-11	3.85e-09
bn141230142	106	74.23	3.43	1.58	57.48	4.3	49.80	16.12	2.73e-11	5.73e-10
bn141202470	7	2.42	2.26	0.03	145.89	60.7	10.11	4.16	1.26e-09	5.52e-08

NOTE—Same as Table 2, but using a search duration of 10 times  $T_{90}$  for long GRBs and 20 s for short GRBs. There is not enough data for the analysis of bn160131174 and bn160515819 for this search duration.

<sup>a</sup> ( $\text{cm}^{-2}\text{s}^{-1}\text{keV}^{-1}$ )

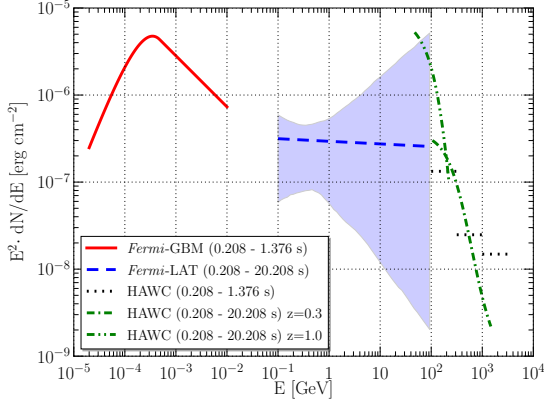


**Figure 5.** Solid line (red) shows the spectrum fitted to the prompt *Fermi*-GBM data of GRB 170206, while dotted lines (black) show the “quasi-differential” limits assuming  $E^{-2}$  obtained from the HAWC data taken during the same time period. Dashed line (blue) shows the best-fit spectrum obtained from the *Fermi*-LAT data in the early afterglow and the shaded area the uncertainty taking into account the correlations and non-linearity of fit parameters. The green dashed-dotted lines show the HAWC limits for two different assumed redshifts.

event). Thus, the non-detection of a GRB within one and a half years of operations is not in conflict with previous estimates.

This paper has presented upper limits for VHE emission from GRBs observed during the first one and a half years of the HAWC Gamma-ray Observatory. None of the bursts was significantly detected. If a SSC component is present in GRB 170206A, the HAWC upper limits constrain the expected cut-off to be less than 100 GeV for reasonable assumptions about the energetics and redshift of the burst. With the current statistics, the limits on the GRB detection rate in HAWC still do not allow strong conclusions about the distribution of the high-energy photon index, high-energy cut-offs or the fraction of GRBs with additional power-law components to be drawn. In order for the limits to become constraining to physical models, more years of operation or a more sensitive analysis are needed. For bursts at high redshift, it is essential to expand the analysis to trigger threshold, ideally with a set of reliable GH separation cuts. It will lower the energy reach of HAWC and thereby improve HAWC’s sensitivity to GRBs. The current search is most sensitive to emission that starts close to the trigger time on the time scales searched. Searches on other time scales and/or start times or a more model-dependent search, e.g. assuming a certain light-curve shape, are possible future avenues to explore. Another possible improvement to the analysis of GBM

burst is to search the error ellipse with a higher containment probability and to take systematic uncertainties into account.

We acknowledge the support from: the US National Science Foundation (NSF); the US Department of Energy Office of High-Energy Physics; the Laboratory Directed Research and Development (LDRD) program of Los Alamos National Laboratory; NASA Fermi GI (grant 81206); Consejo Nacional de Ciencia y Tecnología (CONACyT), México (grants 271051, 232656, 260378, 179588, 239762, 254964, 271737, 258865, 243290, 132197), Laboratorio Nacional HAWC de rayos gamma; L’OREAL Fellowship for Women in Science 2014; Red HAWC, México; DGAPA-UNAM (grants IG100317, IN111315, IN111716-3, IA102715, 109916, IA102917); VIEP-BUAP; PIFI 2012, 2013, PROFOCIE 2014, 2015; the University of Wisconsin Alumni Research Foundation; the Institute of Geophysics, Planetary Physics, and Signatures at Los Alamos National Laboratory; Polish Science Centre grant DEC-2014/13/B/ST9/945; Coordinación de la Investigación Científica de la Universidad Michoacana. Thanks to Luciano Díaz and Eduardo Murrieta for technical support.

G. Vianello is a member of the LAT Collaboration. The *Fermi*-LAT Collaboration acknowledges generous ongoing support from a number of agencies and institutes that have supported both the development and the operation of the LAT as well as scientific data analysis. These include the National Aeronautics and Space Administration and the Department of Energy in the United States; the Commissariat à l’Energie Atomique and the Centre National de la Recherche Scientifique / Institut National de Physique Nucléaire et de Physique des Particules in France; the Agenzia Spaziale Italiana and the Istituto Nazionale di Fisica Nucleare in Italy; the Ministry of Education, Culture, Sports, Science and Technology (MEXT), High Energy Accelerator Research Organization (KEK) and Japan Aerospace Exploration Agency (JAXA) in Japan; and the K. A. Wallenberg Foundation, the Swedish Research Council and the Swedish National Space Board in Sweden. Additional support for science analysis during the operations phase is gratefully acknowledged from the Istituto Nazionale di Astrofisica in Italy and the Centre National d’Études Spatiales in France.

*Software:* ROOT (Brun & Rademakers 1997), GammaPy (Donath et al. 2016), Matplotlib (Hunter 2007), NumPy (Van Der Walt et al. 2011), SciPy (Jones et al. 2001–)

## REFERENCES

- Abdo, A. A., Ackermann, M., Ajello, M., et al. 2009, *ApJL*, 706, L138
- . 2010, *ApJ*, 712, 558
- Abeysekara, A. U., Aguilar, J. A., Aguilar, S., et al. 2012, *APh*, 35, 641
- Abeysekara, A. U., Alfaro, R., Alvarez, C., et al. 2015, *ApJ*, 800, 78
- Abeysekara, A. U., Albert, A., Alfaro, R., et al. 2017, *ApJ*, 843, 39
- Acciari, V. A., Aliu, E., Arlen, T., et al. 2011, *ApJ*, 743, 62
- Ackermann, M., Asano, K., Atwood, W. B., et al. 2010, *ApJ*, 716, 1178
- Ackermann, M., Ajello, M., Asano, K., et al. 2013, *ApJS*, 209, 11
- Ackermann, M., Ajello, M., Asano, K., et al. 2014, *Sci*, 343, 42
- Aharonian, F., Akhperjanian, A. G., Barres de Almeida, U., et al. 2009a, *A&A*, 495, 505
- . 2009b, *ApJ*, 690, 1068
- Albert, J., Aliu, E., Anderhub, H., et al. 2007, *ApJ*, 667, 358
- Asano, K., Guiriec, S., & Mészáros, P. 2009, *ApJL*, 705, L191
- Atwood, W. B., Abdo, A. A., Ackermann, M., et al. 2009, *ApJ*, 697, 1071
- Band, D., Matteson, J., Ford, L., et al. 1993, *ApJ*, 413, 281
- Böttcher, M., & Dermer, C. D. 1998, *ApJL*, 499, L131
- Brun, R., & Rademakers, F. 1997, *NIMPA*, 389, 81
- Connaughton, V., Briggs, M. S., Goldstein, A., et al. 2015, *ApJS*, 216, 32
- Donath, A., Deil, C., Arribas, M. P., et al. 2016, in *Proc. 34th ICRC (The Hague)*, 789
- Fana Dirirsa, F., Tak, D., Vianello, G., Racusin, J., & Kocevski, D. 2017, *GCN*, 20617
- Feldman, G. J., & Cousins, R. D. 1998, *PhRvD*, 57, 3873
- Fraija, N., Lee, W. H., Veres, P., & Barniol Duran, R. 2016, *ApJ*, 831, 22
- Galama, T. J., Vreeswijk, P. M., van Paradijs, J., et al. 1998, *Nature*, 395, 670
- Galli, A., & Guetta, D. 2008, *A&A*, 480, 5
- Gilmore, R. C., Somerville, R. S., Primack, J. R., & Domínguez, A. 2012, *MNRAS*, 422, 3189
- Granot, J., & Guetta, D. 2003, *ApJL*, 598, L11
- Guetta, D., & Granot, J. 2003, *ApJ*, 585, 885
- Guiriec, S., Kouveliotou, C., Daigne, F., et al. 2015, *ApJ*, 807, 148
- Hunter, J. D. 2007, *CSE*, 9, 90
- Inoue, S., Granot, J., O’Brien, P. T., et al. 2013, *APh*, 43, 252
- Jones, E., Oliphant, T., Peterson, P., et al. 2001–, *SciPy: Open source scientific tools for Python*, , [Online; accessed 2017-01-18]. <http://www.scipy.org/>
- Klebesadel, R. W., Strong, I. B., & Olson, R. A. 1973, *ApJL*, 182, L85
- Kouveliotou, C., Meegan, C. A., Fishman, G. J., et al. 1993, *ApJL*, 413, L101
- Kruehler, T., de Ugarte Postigo, A., Malesani, D., & Kuutma, T. 2016, *GCN*, 19164
- Lennarz, D., & Taboada, I. 2016, in *Proc. 34th ICRC (The Hague)*, 715
- Lennarz, D., & Taboada, I. 2016, *GCN*, 19423
- Lennarz, D., Taboada, I., & Wood, J. 2017, in *Proc. Gamma 2016 (Heidelberg)*, Vol. 1792, 050033
- Malesani, D., Kruehler, T., Xu, D., et al. 2015, *GCN*, 17755
- Mattox, J. R., Bertsch, D. L., Chiang, J., et al. 1996, *ApJ*, 461, 396
- Meegan, C., Lichti, G., Bhat, P. N., et al. 2009, *ApJ*, 702, 791
- Narayan, R., Paczynski, B., & Piran, T. 1992, *ApJL*, 395, L83
- Nemiroff, R. J. 1994, *Comments on Astrophysics*, 17, 189
- Neyman, J., & Pearson, E. S. 1928, *Biometrika*, 20, 175
- O’Brien, P. T., Willingale, R., Osborne, J., et al. 2006, *ApJ*, 647, 1213
- Paczynski, B. 1991, *AcA*, 41, 257
- Patrignani, C., Agashe, K., Aielli, G., et al. 2016, *ChPhC*, 40, 100001
- Piran, T. 1999, *PhR*, 314, 575
- Razzaque, S., Dermer, C. D., & Finke, J. D. 2010, *OAJ*, 3, 150
- Sari, R., & Esin, A. A. 2001, *ApJ*, 548, 787
- Selsing, J., Vreeswijk, P. M., Japelj, J., et al. 2016, *GCN*, 19274
- Taboada, I., & Gilmore, R. C. 2014, *NIMPA*, 742, 276
- Van Der Walt, S., Colbert, S. C., & Varoquaux, G. 2011, *CSE*, 13, 22
- Vernetto, S. 2000, *APh*, 13, 75
- Vianello, G., Yassine, M., & Moretti, E. 2016, *GCN*, 19158
- Weekes, T. C., Cawley, M. F., Fegan, D. J., et al. 1989, *ApJ*, 342, 379
- Woosley, S. E. 1993, *ApJ*, 405, 273



**Table 7.** Data of LAT-detected GRBs

	Time UTC	R.A. J2000	Decl. J2000	Error (deg)	Zen (deg)	$T_{90}$ (s)	$T_{90}$ Start (s)
170206A	10:51:57.696	14h11m09.6s	+14d28m48.0s	0.85	11.1	1.168	0.208
160310A	00:22:58.468	06h35m17.33s	-07d12m56.0s	1.389E-4	34.3	18.173	0.003
150416A	18:33:25.965	03h55m00.0s	+52d57m36s	1.9300	42.7	33.281	0.512

NOTE—The three GRBs detected by LAT that are analysed in this paper.

## APPENDIX

### A. GRB SELECTION

GRBs occurring in the field of view of HAWC (down to a zenith angle of  $51^\circ$ ) are found using the online tables for *Fermi*-LAT<sup>2</sup>, *Fermi*-GBM<sup>3</sup> and *Swift*<sup>4</sup> (Tables 7–9). The GRBOX: Gamma-Ray Burst Online Index<sup>5</sup> was additionally searched for GRBs from other experiments, but no matches were found.

For the *Fermi*-LAT-detected GRBs, the trigger time,  $T_{90}$  and  $T_{90}$  Start, are taken from the *Fermi*-GBM catalogue. For GRB 170206A, the position and error stem from the best on-ground location of the LAT detector (Fana Dirirsa et al. 2017). For GRB 160310A, the position is taken from NOT optical observations (Kruehler et al. 2016). GRB 150416A was only located by *Fermi*-GBM, so its position and error are taken from the *Fermi*-GBM catalogue.

The *Swift* position is, in order of preference, the UVOT, XRT, or BAT position. For the *Swift* / *Fermi*-GBM co-detection, the burst is analysed using the *Swift* information.

<sup>2</sup> [http://fermi.gsfc.nasa.gov/ssc/observations/types/grbs/lat\\_grbs/](http://fermi.gsfc.nasa.gov/ssc/observations/types/grbs/lat_grbs/)

<sup>3</sup> <https://heasarc.gsfc.nasa.gov/W3Browse/all/fermigbrst.html>

<sup>4</sup> [http://swift.gsfc.nasa.gov/archive/grb\\_table/](http://swift.gsfc.nasa.gov/archive/grb_table/)

<sup>5</sup> <http://www.astro.caltech.edu/grbox/grbox.php>

**Table 8.** Data of *Swift*-detected GRBs

	Trigger Number	Time UTC	R.A. J2000	Decl. J2000	Zenith (deg)	BAT $T_{90}$ (s)	Redshift
160410A	682269	05:09:48	10h02m44.37s	03d28m42.7s	31.6	8.2	1.717 <sup>a</sup>
151228B	668641	22:47:14	22h57m41.87s	08d04m53.7s	11.2	48.0	n/a
151205A	666352	15:46:00	15h17m09.27s	35d44m38.4s	21.9	62.8	n/a
150817A	652334	02:05:13	16h38m31.47s	-12d03m10.6s	32.4	38.8	n/a
150811A	651882	04:06:09	19h25m21.40s	-15d25m31.1s	35.3	34.00	n/a
150716A	649157	07:06:43	18h33m57.10s	-12d58m48.9s	40.0	44	n/a
150710A	648437	00:28:02	12h57m52.91s	14d19m05.0s	5.4	0.15	n/a
150530B	GA	13:28:38	00h29m59.04s	44d17m24.0s	28.3	n/a	n/a
150530A	642018	11:42:18	21h50m02.94s	57d30m59.8s	38.6	6.62	n/a
150527A	641698	06:48:55	19h15m50.32s	04d12m06.9s	41.5	112	n/a
150428A	639275	01:30:40	12h34m09.22s	06d57m13.2s	47.9	53.2	n/a
150423A	638808	06:28:04	14h46m18.96s	12d17m00.6s	12.6	0.22	1.394 <sup>b</sup>
150323B	GA	09:28:38	17h21m48.83s	38d19m04.6s	36.1	~60	n/a
150317A	635148	04:22:42	09h15m56.32s	55d27m56.6s	36.5	23.29	n/a
150302A	633237	05:42:36	11h42m07.48s	36d48m39.8s	30.0	23.74	n/a
150211A	630714	11:52:11	16h59m26.21s	55d23m36.2s	44.0	13.6	n/a
150203A	629578	04:09:07	06h33m35.80s	06d57m13.4s	12.1	25.8	n/a
141205A	GA	08:05:17	06h11m26.16s	37d52m33.6s	19.4	1.1	n/a

NOTE—The 18 *Swift*-detected GRBs in the HAWC field of view that are analysed in this paper.

GA means the burst was found in a ground analysis. For GRB 150530B, a  $T_{90}$  of 20 s is assumed.

<sup>a</sup>Selsing et al. (2016)

<sup>b</sup>Malesani et al. (2015), redshift only tentative

**Table 9.** Data of *Fermi*-GBM-detected GRBs

	Time UTC	R.A. J2000	Decl. J2000	Error (deg)	Zen (deg)	GBM $T_{90}$ (s)	$T_{90}$ Start (s)
bn160605847	20:19:29.764	07h23m55.2s	-19d49m48s	4.9500	39.8	5.504	-0.064
bn160527080	01:55:37.323	14h33m43.2s	+06d40m48s	6.5500	42.6	25.344	-18.688
bn160521839	20:07:53.873	04h50m02.4s	-13d42m00s	4.4400	34.7	15.872	-0.768
bn160515819	19:38:41.037	05h22m16.8s	-16d18m36s	3.4300	36.5	84.481	-0.768
bn160406503	12:04:36.798	17h27m11.3s	+32d15m47s	11.8000	20.3	0.432	-0.336
bn160315739	17:44:50.341	21h19m38.4s	-22d06m36s	23.0500	46.6	3.328	-2.816
bn160303201	04:49:32.084	10h53m57.6s	+56d56m24s	9.0500	42.9	48.129	1.792
bn160301215	05:10:18.519	07h37m36.0s	+02d17m24s	3.4800	29.7	29.697	0.256
bn160228034	00:48:52.491	02h08m50.4s	+39d22m48s	12.4300	39.8	16.128	-12.544
bn160220868	20:50:12.110	21h47m33.6s	+06d03m00s	15.7800	39.5	22.528	-7.424
bn160215773	18:33:30.387	23h47m09.6s	+01d43m48s	3.4400	34.6	141.314	54.273
bn160211119	02:50:48.276	08h12m48.0s	+53d25m48s	4.9700	44.9	0.960	-0.768
bn160206430	10:19:12.431	12h17m02.4s	+52d24m36s	4.1700	34.1	21.504	-5.632
bn160131174	04:09:56.714	07h32m07.2s	+15d29m24s	4.7100	17.8	205.315	-0.768
bn160118060	01:25:42.450	01h10m52.8s	+59d46m48s	1.4900	44.1	46.849	1.024
bn160113398	09:32:30.524	12h29m02.4s	+11d31m48s	1.2000	29.2	24.576	26.176
bn160107931	22:20:41.502	19h58m40.8s	+06d24m47s	0.1700	45.4	113.922	-11.520
bn160102500	11:59:22.628	14h55m04.8s	+06d22m48s	5.8100	40.8	25.344	-12.032
bn151129333	08:00:06.085	04h03m16.8s	-11d29m24s	5.6700	42.2	52.224	-32.768
bn151030999	23:58:22.637	19h50m31.2s	+30d51m00s	1.0000	12.3	116.482	6.144
bn151023104	02:29:25.137	23h58m57.6s	-17d09m00s	16.4000	45.8	10.240	-2.304
bn151022577	13:51:02.089	07h21m28.8s	+40d13m48s	21.3600	33.6	0.320	-0.160
bn150928359	08:37:19.023	05h35m07.2s	+34d14m24s	4.5700	42.8	53.504	-30.208
bn150923297	07:07:36.184	21h07m12.0s	+31d49m12s	10.7600	50.3	0.192	-0.112
bn150906944	22:38:47.307	14h08m09.6s	+01d05m24s	5.1900	23.8	0.320	-0.256
bn150904479	11:30:20.956	04h28m19.2s	-20d22m48s	10.8900	40.2	23.296	-4.096
bn150811849	20:22:13.749	12h25m23.5s	-14d06m18s	0.9900	37.8	0.640	-0.064
bn150721242	05:49:08.934	22h16m33.6s	+07d45m36s	1.5000	45.7	18.432	1.024
bn150705588	14:07:11.608	04h26m09.6s	-06d37m12s	12.6000	38.3	0.704	-0.256
bn150622393	09:26:32.023	17h48m12.0s	+33d15m00s	1.0000	44.4	60.673	1.024
bn150522944	22:38:44.068	08h43m26.4s	+58d34m48s	10.4700	40.0	1.024	-0.128
bn150502435	10:25:55.163	16h05m50.4s	+42d03m36s	1.0000	39.2	109.314	5.888
bn150329288	06:55:19.123	10h52m00.0s	-12d19m12s	11.7300	42.9	28.928	-2.560
bn150318521	12:29:53.024	17h56m12.0s	-30d13m12s	2.1900	49.3	94.720	0.768
bn150206407	09:46:27.485	14h42m21.6s	+57d30m00s	6.7600	46.3	5.120	-1.024
bn150201040	00:56:54.289	00h22m31.2s	+19d45m00s	13.9200	39.5	0.512	-0.320
bn150131951	22:49:26.183	04h09m04.8s	+19d16m12s	5.3100	43.9	8.192	-0.256
bn150128791	18:59:14.294	18h09m04.8s	+27d46m48s	3.3200	40.0	85.248	-3.328
bn150126868	20:50:35.778	23h22m00.7s	-12d22m05s	0.5100	32.7	96.513	6.400
bn150110433	10:23:38.232	14h28m00.0s	+18d54m00s	1.0000	46.1	74.304	-1.344
bn150105257	06:10:00.463	08h17m16.8s	-14d46m48s	1.0000	41.7	73.729	3.072
bn141230142	03:24:22.637	03h47m55.2s	+01d35m24s	3.8600	18.0	9.856	0.000
bn141202470	11:17:05.606	09h40m02.4s	+59d52m12s	3.3200	40.8	1.344	-0.064

NOTE—The 43 GRBs detected only by *Fermi*-GBM in the HAWC field of view that are analysed in this paper.